Texture features based microscopic image classification of liver cellular granuloma using artificial neural networks

Texture features based microscopic image classification of liver cellular granuloma using artificial neural networks

Fuqian Shi[1, *], Gaoxiang Chen[1], Yu Wang[1], Ningning Yang[1], Yating Chen[1], Nilanjan Dey[2], and R. Simon Sherratt[3]
1. First Affiliated Hospital of Wenzhou Medical University, Wenzhou 325035, China.
2. Department of Information Technology, Techno India College of Technology, West Bengal 740000, India
3.Department of Biomedical Engineering, the University of Reading, RG6 6AY, UK.
{sfq@wmu.edu.cn, 582372420@qq.com, 710444803@qq.com, 1062764811@qq.com, 582372420@qq.com, nilanjan.dey@tict.edu.in, r.s.sherratt@reading.ac.uk}
*Corresponding author: Fuqian Shi, sfq@wmu.edu.cn

Abstract—Automated classification of Schistosoma mansoni granulomatous microscopic images of mice liver using Artificial Intelligence (AI) technologies is a key issue for accurate diagnosis and treatment. In this paper, three grey difference statistics-based features, namely three Gray-Level Co-occurrence Matrix (GLCM) based features and fifteen Gray Gradient Co-occurrence Matrix (GGCM) features were calculated by correlative analysis. Ten features were selected for three-level cellular granuloma classification using a Scaled Conjugate Gradient Back-Propagation Neural Network (SCG-BPNN) in the same performance. A cross-entropy is then calculated to evaluate the proposed Sigmoid input and the ten-hidden layer network. The results depicted that SCG-BPNN with texture features performs high recognition rate compared to using morphological features, such as shape, size, contour, thickness and other geometry-based features for the classification. The proposed method also has a high accuracy rate of 87.2% compared to the Back-Propagation Neural Network (BPNN), Back-Propagation Hopfield Neural Network (BPHNN) and Convolutional Neural Network (CNN).

Keywords: back-propagation neural network; gray gradient co-occurrence matrix; gray level co-occurrence matrix; microscopic image classification; scaled conjugate gradient

I. INTRODUCTION

Schistosoma mansoni granulomatous is a parasite egg deposited in a host leading to fibrosis diseases due to the mansoni infection. Granulomatous diseases of the liver span a huge range of infectious, drug-related, and immunologic disorders, which have different granulomas types and fibrosis stages [1]. Recently, researchers have conducted several experimental analyses on cellular granuloma of mice liver using high-resolution microscopes, such as cell phase-contrast microscopy and probe-based confocal laser endomicroscopy [2] [3]. Accordingly, image processing has a significant role to separate surrounding tissues based on shape, color and texture analysis to distinguish between normal and abnormal liver cases using the captured microscopic images for further diagnosis [4]. For automated computer-aided diagnosis systems, medical image processing, including image preprocessing, feature extraction and classification have all been developed.

For mice liver cellular granulomatous detection and classification, feature extraction has a significant role to measure and digitalize the inherent nature of the fibrosis regions and their attributes as well as to decompose and symbolize these regions to form the feature vector for further classification. Most researchers have focused on morphological feature based automatic recognition of microscopic images [5], while morphological feature calculations take more of a geometrical analysis on the microscopic images. On the contrary, texture analysis is an important research content for image understanding, analysis, recognition, and description of the difference of the structure, direction, granularity and regularity of the different regions of the microscopic image [6-7]. Moreover, texture contains not only the surface properties/characteristics but also some extent that reflects the relationship between them and the environment. Therefore, the texture features in gray statistical information can reflect the distribution structure and spatial information [8]. For diagnosis and treatment, the feature extraction process is followed by the classification process, where image quantitative analysis is used to calculate the texture of the Region of Interest (ROI) and morphological features, and form a feature vector space for the purposes of classification. In microscopic image classification, an artificial neural network is extensively used for prediction and classification. The artificial neural network has high-speed information processing ability and large knowledge storage capacity, and typical algorithms include the Back-Propagation Neural Network (BPNN), Competitive Kohonen Neural Network (CKNN), Feed-forward Neural Network (FNN) and Hopfield Neural Network (HNN). Hence, artificial neural networks have a significant role in medical image analysis and classification.

For microscopic liver image analysis and classification, Akram *et al*. [9] selected features based on texture and color

properties for further classification of the abnormal liver images using the Support Vector Machine (SVM) to perform classification. The results depicted that the extracted texture-based features with the SVM classifier achieved an accuracy of 83% on a mice liver dataset. Furthermore, Amin and Mahmoud-Ghoneim [10] applied statistical texture analysis approaches, namely run-length matrices and co-occurrence on microscopic images of rats' samples followed by classification using linear discriminant analysis and agglomerative hierarchical clustering. The classification results proved that texture analysis was successful to discriminate between the control and fibrosis groups with 100% sensitivity and specificity. Meng *et al*. [11] implemented texture features based histology image supervised classification and multimodal fusion. Xie *et al*. [12] used tumor color, texture and border features for melanoma classification; Kosmas Dimitropoulos *et al.* [13] used adaptive neuro-fuzzy inference systems for automatic detection of centroblasts (CBs) in microscopic images.

Texture features calculation to find the defects of parameters, such as texture features that are specific to a pathological region has been shown to be difficult and time-consuming using BPNN based classification [14]. Therefore, it becomes necessary to develop techniques, such as conjugate gradient, to overcome this shortcoming. The conjugate gradient method is a special conjugate direction method, also related to the gradient, which utilizes the gradient information of an objective function (the product of the gradient and the direction satisfies the "descent" condition). The conjugate gradient method differs from that in the negative gradient direction of the current point and is conjugate with the search direction in front to obtain a new search direction [15~16]. Chen *et al.* [17] proposed a regularized deep feature extraction method using a Convolutional Neural Network (CNN) for hyperspectral image classification. Geng *et al*. [18] introduced deep supervised and contractive neural network using a Gray Level-Gradient Co-occurrence Matrix (GLGCM). Furthermore, Chen *et al*. [19] used BPNN for recognition on oceanic internal waves based on Gray Gradient Co-occurrence Matrix (GGCM). Yu used an improved LBP algorithm for texture and face classification [20].

In this paper, the gray level co-occurrence matrix (GLCM) is improved according to a weighting coefficient. The redundant features are removed through the analysis of the correlation of texture features of the microscopic image of Schistosoma mansoni based cellular granulomatous of mice liver. The gray-difference based features, GLCM based features, combined with GGCM for cellular granuloma microscopic image of mice liver feature calculations is thus proposed in this paper. Furthermore, a scaled conjugate gradient BPNN (SCG-BPNN) for classification is deployed. The organization of the remaining sections is as follows. Section 2 presents the methods for image classification and the experimental process. Section 3 addresses the results and comparative analysis. Section 4 involves the conclusions of the present study.

II. METHODOLOGY

A. Texture-based Features Extraction

Statistical computation is carried out in regions containing multiple pixels and often has strong resistance to noise. In this work, 21 texture-based features were calculated, including grey difference statistics-based features (mean, contract, and entropy), GLCM (energy, correlation, and inertia moment) and GGCM based features (T1-T15). By correlative analysis, 10 features are then selected as a vector input for the Scaled Conjugate Gradient Back-Propagation Neural Network (SCG-BPNN) [21].

Assume (x, y) is a pixel's coordinates in a microscopic fibrosis image, where $x \in \{1, 2, \ldots, m\}$, and $y \in \{1, 2, \ldots, n\}$, which contains L gray levels. Accordingly, $(x + \Delta x, y + \Delta y)$ is the nearby pixel, where $\Delta x > 0$, and $\Delta y > 0$ as $f(x, y)$ is the intensity value of this pixel. So, the gray value can be calculated by:

$$g_{\Delta}\left(f(x,y)\right) = g\left(f(x,y)\right) - g\left(f(x+\Delta x, y+\Delta y)\right) \tag{1}$$

where g_{Δ} is the gray difference. Thus, for m levels, by counting g_{Δ} in each m, the probability $p(i)$ on each g_{Δ} can be obtained, where $(i = 1, \ldots, m)$.

(1) Gray Difference-based Features

Hence, the features of mean, contract, and entropy are given from [22]:

$$mean = \frac{1}{m}\sum_{i=1}^{m} ip(i) \tag{2}$$

$$contract = \sum_{i=0}^{m} i^2 p(i) \tag{3}$$

$$entropy = -\sum_{i=0}^{m} p(i)\log_2\left(p(i)\right) \tag{4}$$

(2) Gray-level Co-occurrence Matrix-based Features

The GLCM is a common method to describe the texture by examining the spatial correlation characteristics of the gray level. It is based on the statistical analysis of two pixels with a given distance. Intuitively speaking, if the image is constituted with similar blocks of pixels' gray value, the GLCM is diagonal elements with relatively large value; if the pixel gray value change in the local area, then the off-diagonal elements will have relatively large values. The energy, correlation and inertia moment can be calculated as [6, 22, 23]:

$$energy = \sum_{x=0}^{m-1}\sum_{y=0}^{m-1} P_{xy}^2 \tag{5}$$

$$correlation = \frac{1}{\sigma_X \sigma_Y}\sum_{x=0}^{m-1}\sum_{y=0}^{m-1}(x-\mu_X)(y-\mu_Y)P_{xy} \tag{6}$$

$$im = \sum_{i=0}^{L-1}\sum_{j=0}^{L-1}|i-j|^2 P_{ij} \tag{7}$$

where P_{xy} is the probability of point (x, y) in the $i = 1, \cdots, m$ gray level, $\mu_X = \sum_{x=0}^{m-1} x \sum_{y=0}^{m-1} p_{xy}$, $\mu_Y = \sum_{y=0}^{m-1} y \sum_{x=0}^{m-1} p_{xy}$,

$\sigma_x = \sqrt{\sum_{x=0}^{m-1}(x-\mu_X)^2 \sum_{y=0}^{m-1} p_{xy}}$, and $\sigma_y = \sqrt{\sum_{y=0}^{m-1}(y-\mu_Y)^2 \sum_{x=0}^{m-1} p_{xy}}$, which are the variances and the standard deviations at both the x and y pixel location.

For rough texture, P_{ij} are close to main diagonal, so that im is smaller, while for fine texture, im is larger.

(3) Gray Gradient Co-occurrence Matrix

The GGCM includes the extracted texture features by using gray and gradient synthetic information, which is similar in process to the GLCM. The Sobel operator may be applied to $f(x,y)$ and let $g(x,y)$ refer to gray that have the digitized form $G(x,y)$, thus the new gray L_g is used to calculate the new gray image $G(x,y)$ as:

$$G(x,y) = \frac{g(x,y) - \min(g(x,y))}{\max(g(x,y)) - \min(g(x,y))}(L_g - 1) \qquad (8)$$

The gray gradient co-occurrence matrix H_{ij} is defined as number of $\{(x,y) \mid f(x,y) = 0, G(x,y) = j\}$, which has the normalized form of:

$$\|H_{ij}\| = \frac{H_{ij}}{\sum_{i=0}^{L-1}\sum_{j=0}^{L-1} H_{ij}} \qquad (9)$$

According to $\|H_{ij}\|$, 15 features are defined and extracted as reported in TABLE I [19]. The features mentioned above were then normalized and organized as an input vector for classification using SCG-BPNN, while the target used fewer features under the same performance by SCG-BPNN.

B. Scaled Conjugate Gradient Back-propagation Neural Network

The BPNN is a multilayer network with the Widrow-Hoff learning algorithm and nonlinear differentiable transfer function. A typical Back-Propagation (BP) network uses a gradient descent algorithm, defined by the Widrow-Hoff algorithm. It is a method for computing the gradient of a nonlinear multilayer network [24]. The input of the J^{th} output layer unit is:

$$\text{net}c_J = \sum_{J=1}^{P} W_y b_J \qquad (10)$$

where the actual output is given by:

$$C_J = f(netc_J) \qquad (11)$$

The weighted input of the hidden layer unit I is given by:

$$netb_I = \sum_{k=1}^{n} v_y a \qquad (12)$$

Thus, the actual output of the unit I is:

$$b_I = f(netb_I) \qquad (13)$$

where f is a differential decreasing function, given by:

$$f(x) = \frac{1}{1+e^{-x}} \qquad (14)$$

The algorithm of these steps is described in Algorithm 1.

Algorithm 1: Proposed BPNN

Step 1: Initialize the network and learning parameters, such as setting the initial weights of the network, and learning factors

Step 2: Provide training mode, and training network to meet the learning requirements.

Step 3: Process the forward propagation as follows:

(1) the input mode for a given training mode

(2) the output of the network model

(3) compared with the desired model

(4) If the error occurs, then go to **Step 4**; otherwise, return to **Step 2**.

Step 4: Process the backward propagation steps:

(1) calculates the error of the same cell;

(2) corrects the weights and thresholds;

(3) returns to **Step 2**

To guarantee fast/accurate convergence of the neural networks, the Scaled Conjugate Gradient (SCG) algorithm was applied. The conjugate gradient method uses the first derivative information, but overcomes the disadvantage of slow convergence of the steepest descent method. Additionally, it avoids the need to store and compute the Hesse matrix and the shortcomings of the inverse of the Newton method. It only requires a small storage capacity and provides fast convergence and high stability without any external parameters. However, the SCG uses second order information from the NN but requires only $O(N)$ memory usage, where N is the number of weights in the network.

The performance of SCG was benchmarked against the performance of the standard BP, the Conjugate Gradient Back-propagation (CGB) algorithm and the one-step Broyden-Fletcher-Goldfarb-Shanno memoryless quasi-Newton algorithm (BFGS) [15]. The SCG process is described in Algorithm 2. The used pseudo-code is given in Algorithm 3.

Algorithm 2: Scaled conjugate gradient (SCG) algorithm

Step 1: Given an initial iterates $X^{(0)}$ and precision of iterative coefficient h

Step 2: Let negative gradient of $X^{(0)}$ be the search direction: $S^{(0)} = -\Delta f(X^{(0)})$

Step 3: One dimensional search via $S^{(k)}$ as $X^{(k+1)} = X^{(k)} + \alpha^{(k)} S^{(k)}$

Step 4: Check convergence:

If $\| \Delta f(X^{(k+1)}) \| \le h$ then

$X^* = X^{(k+1)}$; $f(X^*) = f(X^{(k+1)})$

Output optimization solution; go to End.

Else go to **Step 5**

Step 5: If $k = n$ then let $X^{(0)} = X^{(k+1)}$, go to **Step 2**

Else go to **Step 6**

Step 6: Construct new gradient direction

$$\beta = \frac{\| \Delta f(x(k+1)) \|^2}{\| \Delta f(X(k)) \|^2}$$

$$S^{(k+1)} = -\Delta f(X^{(k)}) + \beta^{(k)} S^{(k)}$$

$k = k+1$ go to **Step 3**

Algorithm 3: GGCM H- matrix Calculation

INPUT: image file, grey
OUTPUT: H basic-normalized scale matrix

```
IN←imread('D1_03.png'); % image input
Imshow (IN)
gray←256;
[R, C]←size (IN)
% Calculating gradients matrix using square sum
GM←zeros (R-1, C-1)
FOR i (1 to R-1)
   FOR j (1 to C-1)
      n_GM←(IN (i, j+1)-IN(i,j))^2+(IN(i+1,j)-
IN(i,j))^2
      GM(i,j)←sqrt(double(n_GM))
   ENDFOR
ENDFOR
// Minimum and maximum
n_min←min (GM (:));
n_max←max (GM (:));
// Discrete the gray level of the gradient image
// Set new gray as new_gray
new_gray←32;
// Let new gradient matrix be new_GM
new_GM←zeros (R-1, C-1);
new_GM←uint8((GM-n_min)/(n_max-n_min) *
(new_gray-1))
// Gray gradient co-occurrence matrix calculation
//The gradient matrix is 1 less than the gray scale matrix
and ignores the most outlying of the gray scale matrix
H←zeros (gray, new_gray)
FOR i (1 to R-1)
   FOR j (1 to C-1)
      H(IN(i,j)+1,new_GM(i,j)+1)← H(IN(i,j)+1,
new_GM(i,j)+1)+1
   ENDFOR
ENDFOR
// Let normalized gray gradient matrix be H_basic
Total←i*j
H_basic←H/total
```

III. Results and Discussion

In the current study, microscopic images of magnification 3400 were acquired and examined in the Medical Parasitology Department, Faculty of Medicine, Tanta University, Egypt. These acquired liver samples from normal and Schistosomiasis mansoin infected mice are illustrated in Fig. 1. Some representative images of histopathological samples are obtained from the control liver group; fibrosis and granuloma are illustrated in Fig. 1(a)–(c). Fig. 1(a) demonstrated that the histological analysis of healthy liver shows a normal liver lobular architecture, while the liver fibrosis in Fig. 1(b) has disruption of the tissue architecture, the extension of fibers, and fibers accumulation. In addition, the liver granuloma in Fig. 1(c) shows multinucleated giant cells and lymphocytes or a conglomeration of smaller granulomas. Images were encoded at 24-bits per pixel on red, green, and blue channels.

The colored images were processed using Matlab (version 2017a) to create grey level images of size 256*3*256 and to compute the gradient vectors matrices. To increase the dataset size, each healthy liver image was divided into two sub-images of 256*3*128 size. Thus, 20 images of each class were used in this study. The training phase used 30 images (10 of each class) and the test phase used the rest of 30 images.

A. Features Calculation

Mean (M), Contract (Co), Entropy (E), Energy (En), Correlation (C), and Inertia Moment (IM) of 30 images were calculated and shown in Table 1. The four directions of 0, 45, 90, and 135 on En, C, and IM were calculated and the mean of these four directions was adopted for the next step. The GGCM features in Tables 2-4 list the 1st, 2nd, and 3rd level-fibro cellular granuloma.

B. Training process

A ten-hidden layer NN design with three grey difference statistics-based feature (M, Co, E), three gray-level co-occurrence matrix-based features (En, C, IM), and gray gradient co-occurrence matrix-based features (T1-T15) was constructed. There were 21 features of images, 3200 data applied. Thus, the input matrix is 21*3200, and the target matrix is 3*3200, in which 1st level-fibro cellular granuloma is $[1,0,0]^T$, 2nd level-fibro cellular granuloma is $[0,1,0]^T$, and the 3rd level-fibro cellular granuloma is $[0,0,1]^T$. The cross-entropy was performed with the proposed SCG-BPNN training process as shown in Fig. 2. Setting 70% of data for training (2240 records), was presented to the network during training, and the network was adjusted according to its error; 15% for validation (480 records), which is used to measure network generalization, and to halt training when generalization stops improving; and 15% for testing (480 records), which is to provide an independent measure of network performance during and after training as shown in Fig. 3 [25].

Fig. 1. Samples from the three levels of cellular granuloma microscopic images of mice liver, where (a) first level-fibro cellular granuloma, (b) second level-fibro cellular granuloma, and (c) third level-fibro cellular granuloma.

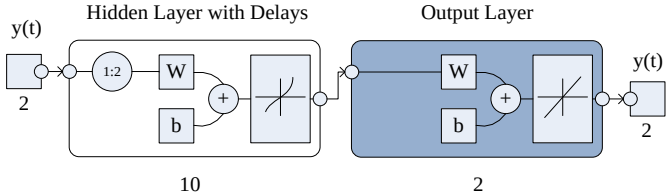

Fig. 2. 10 hidden layers BPNN using SCG.

Table 1 GLCM Features' value of three classifications

Images	Mean(M)	Contract (Co)	Entropy (E)	Energy (En)	Correlation (C)	Inertia Moment (IM)
A1	0.5846	2.27E+04	5.9544	0.0205	0.8963	2.5124
A2	0.549	2.01E+04	5.9662	0.0214	0.9061	3.5518
A3	0.5728	2.18E+04	5.9897	0.0201	0.8857	2.8477
A4	0.5474	2.00E+04	5.9863	0.0187	0.9063	3.2446
A5	0.5516	2.01E+04	5.2921	0.0443	0.9440	0.8211
A6	0.5508	2.01E+04	5.5094	0.0344	0.9400	1.9194
A7	0.5935	2.33E+04	5.6296	0.0359	0.9148	1.3437
A8	0.6669	2.92E+04	4.8391	0.0453	0.9684	0.5520
A9	0.5909	2.30E+04	5.3227	0.0359	0.9404	1.2386
A10	0.5029	1.68E+04	5.6044	0.0263	0.9174	2.7570
B1	0.5737	2.18E+04	5.8114	0.0223	0.9184	2.4489
B2	0.5116	1.73E+04	5.1946	0.0353	0.9442	1.1807
B3	0.5505	2.01E+04	5.5709	0.0245	0.9296	1.9294
B4	0.5551	2.04E+04	5.7232	0.0219	0.9124	2.4392
B5	0.5675	2.13E+04	5.4361	0.0264	0.9358	1.6751
B6	0.5775	2.20E+04	5.6042	0.0284	0.9194	1.7089
B7	0.5741	2.18E+04	5.7882	0.0216	0.9148	2.2714
B8	0.5574	2.06E+04	5.5938	0.0276	0.9242	2.3149
B9	0.5567	2.06E+04	5.7916	0.0202	0.8831	3.3948
B10	0.5366	1.91E+04	5.6746	0.0240	0.9223	2.6020
C1	0.5103	1.76E+04	6.4062	0.0176	0.7574	5.5554
C2	0.4928	1.64E+04	6.2778	0.0209	0.7753	4.9723
C3	0.4978	1.69E+04	6.5513	0.0162	0.7270	6.2586
C4	0.5263	1.87E+04	6.3818	0.0149	0.7163	5.3177
C5	0.5113	1.78E+04	6.5959	0.0145	0.6927	7.2491
C6	0.5217	1.83E+04	6.3612	0.0197	0.7039	5.3325
C7	0.5216	1.82E+04	6.0952	0.0247	0.8114	3.8107
C8	0.4977	1.69E+04	6.5391	0.0164	0.6755	6.9137
C9	0.5084	1.75E+04	6.3609	0.0194	0.7469	5.0677
C10	0.4994	1.70E+04	6.5444	0.0149	0.7167	5.1681

Table 2. 1st level-fibro cellular granuloma

T1	A1	A2	A3	A4	A5	A6	A7	A8	A9	A10
T1	0.3019	0.3139	0.3024	0.3152	0.3294	0.3257	0.3141	0.3364	0.3248	0.3390
T2	15.5918	15.3242	15.6748	14.6702	10.7114	12.3308	12.9371	9.2091	12.1174	13.3615
T3	48666.9506	60813.9609	48886.0521	53214.4055	60096.4041	53995.5007	59367.6702	51247.4335	54294.4579	73663.4528
T4	1912331.3988	2016587.3570	1950295.7037	1879498.2690	1302821.3737	1488417.5935	1433212.6591	1282583.9918	1419916.1481	1752166.1768
T5	0.0011	0.0026	0.0011	0.0018	0.0009	0.0011	0.0009	0.0008	0.0009	0.0035
T6	105.5963	114.8666	103.9456	109.8143	101.2361	98.2116	96.8497	115.6000	105.9825	117.0239
T7	15.5918	15.3242	15.6748	14.6702	10.7114	12.3308	12.9371	9.2091	12.1174	13.3615
T8	57.2349	69.7490	58.3750	68.3788	45.4182	59.3752	46.3586	52.3749	53.7958	71.3283
T9	13.2476	13.4091	13.2915	13.2480	11.1861	12.2821	12.2932	10.1674	12.0661	12.9066
T10	-111.5312	-206.1009	-123.9672	-104.1345	-9.1072	-3.0095	-44.2040	-50.1271	-10.8259	-155.0087
T11	2.3345	2.3310	2.3326	2.3464	2.2555	2.3066	2.2602	2.3081	2.2974	2.3194
T12	0.9691	0.9452	0.9604	0.9744	1.1261	1.0684	1.0835	1.1341	1.0891	1.0085
T13	3.2876	3.2281	3.2747	3.2829	3.3727	3.3461	3.3356	3.4238	3.3682	3.2780
T14	11775.2088	15365.6265	11623.9618	14111.8418	10364.4484	11057.7967	9429.9789	14065.2696	11871.8984	16310.2245
T15	0.0083	0.0109	0.0095	0.0131	0.0029	0.0076	0.0052	0.0012	0.0037	0.0106

Tables 3. 2nd level-fibro cellular granuloma

T1	B1	B2	B3	B4	B5	B6	B7	B8	B9	B10
T1	0.3086	0.3142	0.3199	0.3102	0.3150	0.3131	0.3054	0.3293	0.3246	0.3314
T2	14.2179	12.1362	13.1355	14.0665	12.8627	13.5024	14.2457	13.2809	14.1569	13.7770
T3	47471.7426	52280.3008	51809.5428	48676.1086	52538.3466	52287.9610	47559.9637	59497.6592	57677.1244	64358.5400
T4	1690970.5634	1355140.5665	1536245.5592	1649390.1181	1437381.0482	1523692.4917	1637523.8702	1646636.8041	1771055.6159	1780784.7645
T5	0.0010	0.0009	0.0013	0.0011	0.0011	0.0009	0.0009	0.0021	0.0021	0.0028
T6	105.2023	104.3330	114.8417	106.4662	105.0355	102.4853	105.1254	106.3970	116.4003	115.0945
T7	14.2179	12.1362	13.1355	14.0665	12.8627	13.5024	14.2457	13.2809	14.1569	13.7770
T8	62.1734	58.1669	61.5291	61.1262	58.5088	53.8183	59.3140	67.2009	65.6223	69.0537
T9	12.9438	11.9675	12.5391	12.8662	12.2912	12.5619	12.8598	12.7302	13.0260	13.0237
T10	-51.0151	-20.1204	-48.5817	-56.4202	-44.0639	-25.8506	-60.6437	-92.3635	-127.3191	-130.2682
T11	2.3454	2.3147	2.3329	2.3392	2.3152	2.3102	2.3408	2.3217	2.3324	2.3277

T12	1.0162	1.1017	1.0574	1.0280	1.0810	1.0604	1.0299	1.0316	1.0025	0.9988
T13	3.3391	3.3880	3.3610	3.3432	3.3731	3.3571	3.3522	3.3137	3.2961	3.2809
T14	12413.2483	11986.6066	14384.3877	12552.4968	12158.3096	11023.8733	12063.9336	13533.3587	15184.3276	15463.8116
T15	0.0091	0.0050	0.0052	0.0086	0.0066	0.0059	0.0083	0.0109	0.0076	0.0093

Table 4. 3rd level-fibro cellular granuloma

T1	C1	C2	C3	C4	C5	C6	C7	C8	C9	C10
T1	0.3111	0.3168	0.3101	0.2995	0.3037	0.3068	0.3066	0.3002	0.3022	0.2985
T2	16.7161	16.1987	17.3973	17.1418	17.5933	16.8010	15.3368	17.5719	16.8337	17.4637
T3	9173.0569	9215.6099	9269.3695	7711.2967	7637.8552	8235.4866	10043.9520	7975.3021	9375.5377	6902.9449
T4	419324.6869	370394.6909	450648.6879	350891.7553	411413.7763	365925.4825	353987.2040	413205.5556	428587.4277	359326.2402
T5	0.0021	0.0023	0.0025	0.0015	0.0021	0.0015	0.0014	0.0017	0.0015	0.0016
T6	110.5868	110.2067	116.5026	94.5674	111.8048	94.4182	99.4258	100.8519	99.9060	119.8363
T7	16.7161	16.1987	17.3973	17.1418	17.5933	16.8010	15.3368	17.5719	16.8337	17.4637
T8	63.2031	63.5937	63.2421	53.1304	62.1079	54.4959	58.5130	58.1464	57.8339	52.7525
T9	13.7180	13.6377	13.8599	13.6579	13.8366	13.6584	13.2450	13.7858	13.6211	13.7487
T10	-191.5271	-208.2920	-233.2392	-156.7994	-196.6382	-139.1340	-101.1759	-177.5633	-133.8385	-178.7957
T11	2.3314	2.3186	2.3295	2.3024	2.3376	2.2991	2.3055	2.3193	2.3176	2.3199
T12	0.8608	0.8897	0.8072	0.8580	0.8022	0.8681	0.9699	0.8148	0.8761	0.8268
T13	3.1541	3.1664	3.0936	3.1414	3.1029	3.1432	3.2454	3.1049	3.1672	3.1246
T14	13377.5885	13484.2243	14479.9928	9317.7039	13317.9315	9459.0545	10872.5308	10861.7394	10698.9772	13809.5914
T15	0.0090	0.0090	0.0077	0.0106	0.0085	0.0108	0.0098	0.0101	0.0100	0.0047

Table 5. Predictive accuracy rate with different neural networks

T1	CE	MSE	PAR
BPNN [21]	0.62	0.077	0.855
CNN [27]	0.71	0.068	0.788
BPHNN [23]	0.61	0.066	0.685
FUZZY NN [28]	0.65	0.082	0.752
SCG-BPNN-10	0.67	0.066	0.872
SCG-BPNN-21	0.75	0.071	0.821

Table 6. Comparing to time consuming in large scale dataset (70% for training)

Samples	SCG-BPNN-10	SCG-BPNN-21
1020	0.077	0.62
2050	0.068	0.71
3600	0.066	0.61
5400	0.082	0.65
7200	0.071	0.75
1020	0.066	0.67

By correlative analysis of the features' calculations, especially for texture-based features, M, Co, E, C, IM and T2, T4, T6, T7, T15 were selected as a vector input for the SCG-BPNN by correlative analysis, where the results are illustrated in Fig. 4. The results establish the superiority of the proposed features with the SCG-BPNN classifier. Additionally, the prediction result is very important for NN models. The learning process in fact is to adjust system parameters to make the results more and more accurate, which are the accuracy rate, is to accumulate the "loss" of each sample, and then calculate the average value [24-25].

A comparative study was performed with other related studies using the BPNN, CNN, BPHNN, and fuzzy NN with the proposed methods SGC-BPNN-10 and SGC-BPNN-21. All features are reported in Table 5 showing the Predictive Accuracy Rate (PAR), Cross Entropy (CE) and Mean Squared Error (MSE). The different algorithms listed in TABLE V were used for the same dataset from Section 3.2. It is obvious that the proposed method SCG-BPNN-10 has higher PAR with low MSE. Furthermore, the SCG-BNPP-21 took higher computation time compared to the SCG-BPNN-10 as demonstrated in Table 6.

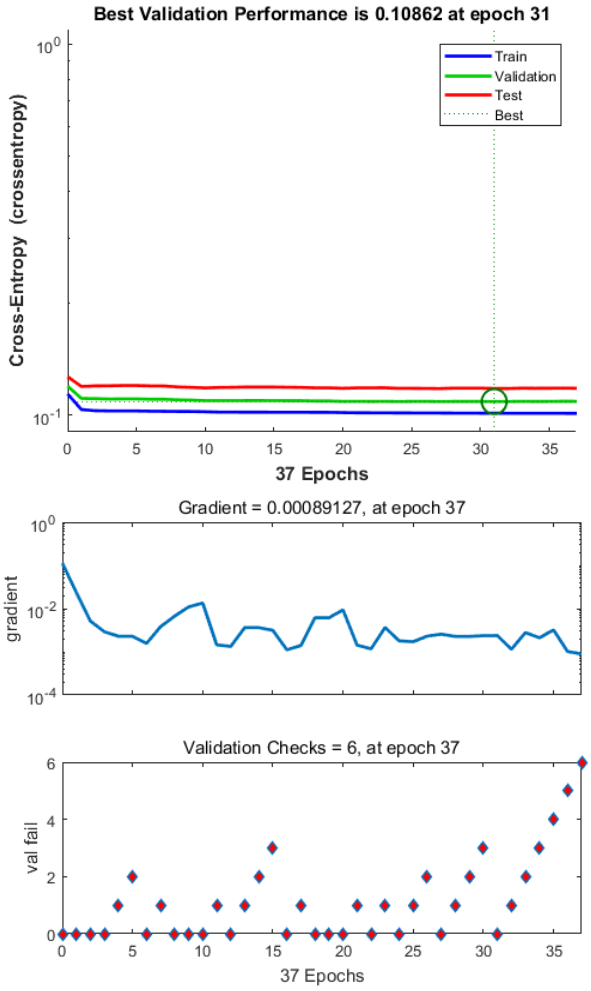

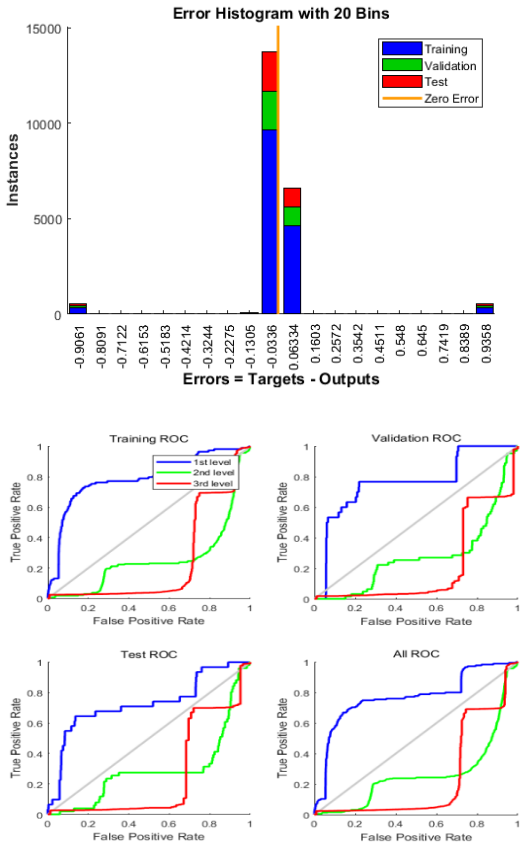

Fig. 3. Performance by epochs, training state, error histogram and receiver operating characteristic with all features.

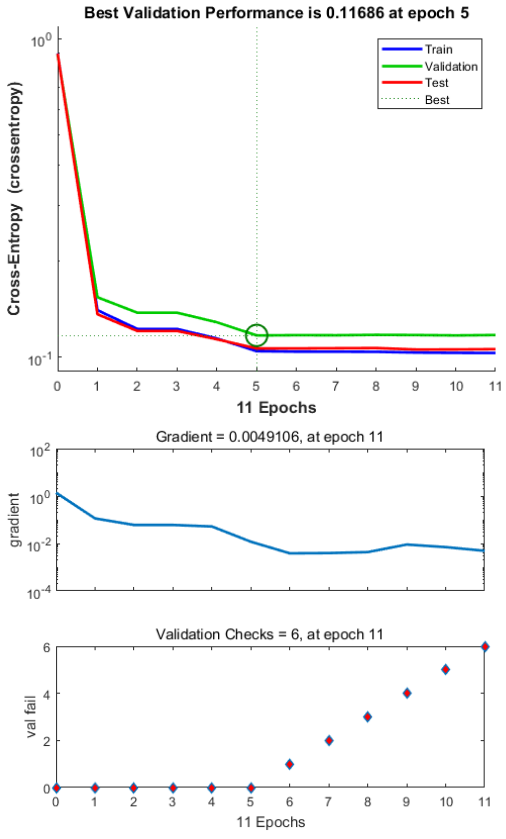

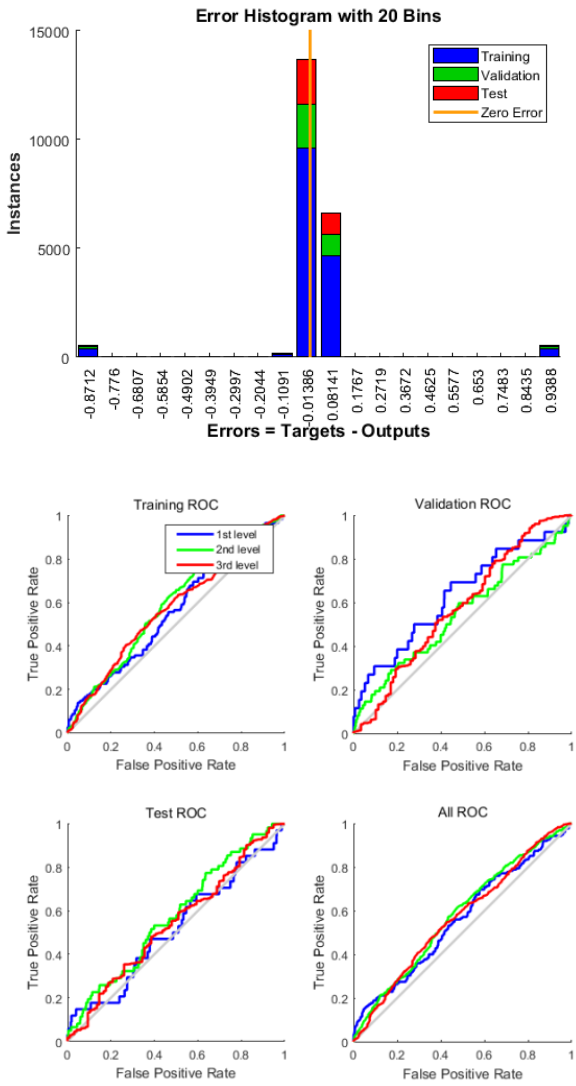

Fig. 4. Performance by epochs, training state, error histogram and receiver operating characteristic with ten features after correlative analysis.

IV. Conclusions

Pathologists primarily use microscopic methods to qualitatively analyze microscopic images of cancer cells by using visual methods. The use of empirical knowledge to diagnose people's health has a significant role in clinical pathology. However, such methods are subjective and consume significant time. Furthermore, the captured microscopic images may be blurred, noisy, have poor contrast, unclear boundary, and human visual fatigue caused by long-term reading. These drawbacks will affect the accuracy of diagnostic analysis and judgment. With the rapid development of computer technology and the maturity of image graphics processing technology, the requirements for detecting objectivity are getting higher and higher, and computer image processing and analysis technology plays an increasingly important role in clinical diagnosis and treatment. The traditional method is to explore the classification, cell counting and texture analysis of precancerous lesions, pathology image retrieval and

management, visualization surgery and reconstruction of human body models. This paper diagnoses diseases by identifying and analyzing microscopic images of diseased cells and can accurately identify and classify microscopic images [26]. The results are as follows:

(1) Realizing the automatic classification of microscopic images of Schistosoma mansoni granuloma using AI technology,

(2) Texture features such as CGCM and GGCM are calculated, and the SCG-BPNN based network training has been verified.

(3) Through cross entropy evaluation, Sigmod input and ten hidden layer network, the training results show that our SCG-BPNN-10 has a high recognition rate with texture features. Compared with BPNN, back-propagation BPHNN and CNN, the proposed method also has higher accuracy.

In the future, insufficient training data, the design of neural network structures, and the definition of loss functions will all be considered.

ACKNOWLEDGMENT

This work is supported by Zhejiang Provincial Natural Science Foundation (Grant no: LY17F030014). Dalia S. Ashour, Assistant Professor of Medical Parasitology and Dina M. Aboraya, Lecturer of Medical Parasitology, Medical Parasitology Department, Faculty of Medicine, Tanta University, Egypt perfumed microscopic experiment and preprocessing the dataset.

REFERENCES

[1] D. E. Kleiner, "Granulomas in the liver," Seminars in Diagnostic Pathology, vol.23, no.3-4, pp.161–169, 2006.

[2] C. H. Huang, S. Sankaran, D. Racoceanu, S. Hariharan, and Sohail Ahmed "Online 3-D tracking of suspension living cells imaged with phase-contrast microscopy," IEEE Trans. Biomed. Eng., vol. 59, no.7, pp.1924–1933, 2012.

[3] W. T. Latt, R. C. Newton, V.S. Marco, C. J. Payne, D. P. Noonan, J. Z Shang, and G. Z. Yang, "A hand-held instrument to maintain steady tissue contact during probe-based confocal laser endomicroscopy," IEEE Trans. Biomed. Eng., vol. 58, no.9, pp.2694–2703, 2011.

[4] F. Zhao, X. X. Li, S. Biswas, R. Mullick, P. R. S. Mendonca and V. Vaidya, "Topological texture-based method for mass detection in breast ultrasound image," in Proc. ISBI, Beijing, China, 2014, pp. 685–689.

[5] J.-P. Thiran, and B. Macq, "Morphological feature extraction for the classification of digital images of cancerous tissues," IEEE Trans. Biomed. Eng., vol.43, no.10, pp.1011–1020, 1996.

[6] D. Choudhury, A. Naug, and S. Ghosh, "Texture and color feature based WLS framework aided skin cancer classification using MSVM and ELM," in Proc. INDICON, New Delhi, India, 2015.

[7] M. Havaei, A. Davy, W. F. David, A. Biard, A. Courville, Y. Bengio, C. Pal, P. M. Jodoin, H. Larochelle, "Brain tumor segmentation with Deep Neural Networks," Medical Image Analysis, vol. 35, pp.18–31, 2017.

[8] D. Schwenninger, K. Moller, H. Liu, and J. Guttmann, "Automated analysis of intratidal dynamics of alveolar geometry from microscopic endoscopy," IEEE Trans. Biomed. Eng., vol. 57, no.2, pp.415–421, 2010.

[9] M. U. Akram, M. A. Khan, M. Naveed, and S. Gul, "Liver image analysis using color and texture descriptors," in Int. Conf. Digital Information Processing, Electronics, and Wireless Communications (DIPEWC2016), Dubai, United Arab Emirates, 2016.

[10] A. Amin, and D. Mahmoud-Ghoneim, "Texture analysis of liver fibrosis microscopic images: a study on the effect of biomarkers," Acta Biochim Biophys Sin, vol. 43, no.3, pp.193–203, 2011.

[11] T. Meng, L. Lin, M. L. Shyu, and S. C. Chen, "Histology image classification using supervised classification and multimodal fusion," in Proc. ISM, Taichung, Taiwan, pp. 145–152, 2010.

[12] F. Y. Xie, H. D. Fan, Y. Li, Z. G. Jiang, R. S. Meng, and A. Bovik, "Melanoma classification on dermoscopy images using a neural network ensemble model," IEEE Trans. Med. Imag., vol. 36, no.3, pp. 849–858, 2017.

[13] Kosmas DimitropoulosEmmanouil MichailTriantafyllia KoletsaIoannis KostopoulosNikos Grammalidis, Using adaptive neuro-fuzzy inference systems for the detection of centroblasts in microscopic images of follicular lymphoma, Signal, Image and Video Processing, vol. 8, pp. 33-40, 2014.

[14] G. Mohan, R. Karthik, P. Swathi Lakshmi, and P. Sajida, "A combinational network for high density noise removal and texture classification using back propagation network," Materials Today: Proceedings, vol. 4, no.8, pp. 7770–7777, 2017.

[15] C. S. Jiang, H. B. Li, and M. Rangaswamy, "On the conjugate gradient matched filter," IEEE Trans. Signal Process., vol. 60, no.5, pp. 2660–2666, 2012.

[16] F. Lenti, F. Nunziata, C. Estatico and M. Migliaccio, "Conjugate gradient method in Hilbert and Banach spaces to enhance the spatial resolution of radiometer Data," IEEE Trans. Geosci. Remote Sens., vol. 54, no.1, pp.397–406, 2016.

[17] Y. S. Chen, H. L. Jiang, C. Y. Li, X.P. Jia, and P. Ghamisi, "Deep feature extraction and classification of hyperspectral images based on convolutional neural networks," IEEE Trans. Geosci. Remote Sens., vol. 54, no.10, pp. 6232–6251, 2016.

[18] J. Geng, H. Y. Wang, J. C. Fan, and X. R. Ma, "Deep supervised and contractive neural network for SAR image classification," IEEE Trans. Geosci. Remote Sens., vol. 55, no. 4, pp. 2442–2459, 2017.

[19] F.-F. Chen, X.-F. Jiang, and Z.-Y. Jiang, "The research of recognition on oceanic internal waves based on gray gradient co-occurrence matrix and BP neural network," in Proc. SOPO, Wuhan, China, 2011.

[20] Wei Yu, Lin Gan, Sha Yang, Yonggang Ding, Pan Jiang, Jun Wang, Shijun Li, An improved LBP algorithm for texture and face classification, vol. 8, pp. 155-161, 2014.

[21] K. R. Singh, and S. Chaudhury, "Efficient technique for rice grain classification using back-propagation neural network and wavelet decomposition," IET Computer Vision, vol. 10, no. 8, pp. 780–787, 2016.

[22] R. M. Haralick, K Shanmugam, and I. Dinstein, "Textural features for image classification," IEEE Trans Syst., Man, and Cybern., vol. 3, no. 6, pp. 610–621, 1973.

[23] L.A. Álvar-Ginés, V.M. Rafael, and E. Kjersti, "Noise robust and rotation invariant framework for texture analysis and classification," Applied Mathematics and Computation, vol. 335, pp. 124–132, 2018.

[24] A. Fakhry, T. Zeng, and S. W. Ji, "Residual deconvolutional networks for brain electron microscopy image segmentation," IEEE Trans. on Med. Imag., vol. 36, no. 2, pp. 447–456, 2017.

[25] D. Wang, T. He, Z. Li, L. Cao, N. Dey, A. S. Ashour, V. E. Balas, P. McCauley, Y. Lin, J. Xu, and F. Shi, "Image features based affective retrieval employing parameter and structure identification improved adaptive neuro fuzzy inference system," Neural Computing and Applications, vol. 29, no. 4, pp. 1087–1102, 2018.

[26] Y. Wang, Y. Chen, N. Yang, L. Zheng, N. Dey, A. S. Ashour, V. Rajinikanth, J. M. R.S. Tavares, and F. Shi, "Classification of Mice Hepatic Granuloma Microscopic Images based on Convolutional Neural Networks", Applied Soft Computing, vol.74, pp. 40-50, 2019